DC Series Arc Fault Detection Method in Photovoltaic System Based on Multiple Frequency Selections for Common-Mode Conductive Voltage

Haining Wang, Xiaozhou Wang, Tao Fan, Jian Wang, Zijie Lin, Yu Shen, Jianhui Su,
and Peng Zhang, *Member, IEEE*

***Abstract*—DC series arc faults are one of the main causes of fire hazards in photovoltaic power systems. The common method of the traditional dc series arc fault detection uses wideband current sensors to obtain the arc current signal, extract arc characteristic frequency components, and make intelligent judgments based on numerous samples. This kind of detection method requires high-performance hardware and has a high cost. This article takes the common-mode conductive voltage (CMCV) signal, which is produced by arc faults, as the object and confirms the feature frequency band of the arc CMCV signal based on the spectral analysis. To obtain the feature frequency component and perform frequency reduction at the hardware level, multiple frequency selection and detection circuits were designed, and the feature quantities of the time and frequency domains were extracted from the output of the circuits. Subsequently, a two-dimensional arc fault feature plane was constructed, and an arc/normal similarity criterion and arc fault judgment algorithm were proposed. Finally, this article discusses or experimentally verifies the effectiveness, reliability, and anti-interference ability of the proposed method. The proposed method is low cost, simple, reliable, and effective and provides a novel idea and approach for dc series arc fault detection.**

***Index Terms*—Arc discharges, electromagnetic conductive interference, fault diagnosis, photovoltaic (PV) power systems, signal detection.**

I. INTRODUCTION

IN RECENT years, photovoltaic (PV) power generation systems have been widely used due to their advantages in meteorological and geographic requirements. Normally, dozens of PV panels are connected in series to boost voltage and obtain high output power, but the high dc voltage means that the dc arcs appear at poor connection spots very easily and cause severe fire hazards. However, dc series arc faults are difficult to distinguish because the changes in the voltage and current of the PV string are not obvious when an arc fault occurs. Therefore, the dc series arc fault detection method has become a debated issue in PV power system applications. To realize fast and accurate dc series arc fault detection, researchers have conducted many trials. In the field of arc current feature extraction, wavelet decomposition has been widely used due to its advantage of representing time–frequency information at multiple scales, which matches the characteristics of arc signal randomness and wide spectrum well. The usual method of extracting features is to use wavelet decomposition to obtain characteristic frequency components and then calculate feature quantities, such as the root-mean-square values of the components, the wavelet transform modulus maximum, and the energy of high-frequency bands [1]–[5]. However, wavelet decomposition requires a well-chosen wavelet basis function, and poor basis function selection may mean that the features of the arc current are not sufficiently obvious to differentiate arc faults. Therefore, it is necessary to select the optimal wavelet basis function selection [6]. In addition to wavelet decomposition, other methods have been proposed to obtain the features of arc current signals, such as the short-time Fourier transform [7], [8], fast Fourier transform (FFT) [9], [10], entropy analysis [11], [12], and ensemble empirical mode decomposition [13], [14]. In terms of fault identification, many kinds of neural networks and intelligent algorithms have been frequently applied, such as convolutional neural networks [15], [16], backpropagation neural networks [6], [17], [18], and artificial intelligence (AI) based or classification algorithms [3], [9], [19]–[21]. These methods have very high accuracy. However, these methods require many samples and much time to be trained well, and high-performance hardware, such as a fast CPU and large memory space, is indispensable. Therefore, other researchers have proposed simple methods using the thresholds of time–frequency features [5], [10], [11], spectrum energy [1], the

---

Manuscript received 6 December 2021; revised 14 April 2022; accepted 17 July 2022. Date of publication 22 July 2022; date of current version 6 September 2022. This work was supported in part by the National Key R&D Program of China under Award 2018YFB1500800, in part by the Technology Project of State Grid Company, Ltd. under Award SGTJDK00DYJS2000148, in part by The Young Teachers Scientific Research and Innovation Launch Special A Project under Grant JZ2021HGQA0192, in part by The Basic Operating Expenses of Central Scientific Research under Award PA2020GDGP0053, and in part by 111 Project under Award BP0719039. Recommended for publication by Associate Editor M. Tavakoli Bina. *(Corresponding author: Xiaozhou Wang.)*

Haining Wang, Xiaozhou Wang, Yu Shen, Jianhui Su, and Peng Zhang are with the Engineering Research Center, Ministry of Education for Photovoltaic System, Hefei University of Technology, Hefei 230009, China (e-mail: ahwhn@126.com; wxz0@qq.com; shenyuxxh@163.com; su_chen@126.com; handanzp@126.com).

Tao Fan is with the State Grid Corporation of China, Beijing 100031, China (e-mail: fan-tao@sgcc.com.cn).

Jian Wang is with the Tianjin Electric Power Company, Tianjin 300384, China (e-mail: 847632578@qq.com).

Zijie Lin is with the Department of Finance, School of Economics and Management, Tsinghua University, Beijing 100190, China (e-mail: zj.lin1@outlook.com).

Color versions of one or more figures in this article are available at https://doi.org/10.1109/TPEL.2022.3193195.

Digital Object Identifier 10.1109/TPEL.2022.3193195

two-dimensional (2-D) Euclidean distance [2], and the entropy of components [14] to distinguish dc series arc faults. However, this kind of method can be easily influenced by the environment and operation conditions, and threshold values are difficult to set.

In general, these studies suffer two problems. First, most researchers choose the dc current signal as the study subject, but the maximum frequency of most current signal analyses is 100 kHz due to the limited current sensor performance. There is much power electronics noise in the 0–100 kHz band, and noise will disturb arc fault detection. Second, all these arc current feature extraction methods and feature identification methods are carried out by a math algorithm. Signal decomposition, characteristic classification, and neural network construction depend on a high-performance processor. In addition, the frequency range of the results of the signal decomposition algorithm is related to the sampling frequency. This means that a fast A/D module is required if researchers want to analyze the high-frequency characteristics of arc fault signals. Therefore, the hardware cost will be increased.

The contributions of this article are listed as follows.

1) This article focuses on the common-mode conductive voltage signal (CMCV signal), which is a kind of electromagnetic interference (EMI) produced by dc series arc faults because the CMCV signal can couple with other networks through conductors directly [22]; hence, the fault signal can be collected without any sensors.
2) To depress the performance requirement of the CPU and A/D module, this article performed multiple frequency selection and detection branches to extract frequency components and realize frequency reduction.
3) The proposed method has the advantages of low cost, fewer sample requirements, and equivalent accuracy compared with common arc fault detection methods. Anti-interference ability and load or irradiation changes will not affect the effectiveness of the proposed detection method.

The rest of this article is organized as follows. Section II illustrates the feasibility of detecting arc faults through CMCV signals in PV systems and analyzes the characteristics of CMCV signals. Section III describes the design of multiple frequency selection and detection branches. Section IV is the proposition of the similarity criterion and detection algorithm. Section V presents the verification and discussion of the proposed method. Finally, Section VI concludes this article.

II. CHARACTERISTICS OF THE CMCV SIGNAL IN THE PV SYSTEM

A. *Feasibility of the Detection Method Based on the CMCV Signal*

A common PV power system is a floating ground, and there is a stray capacitance between the dc system and ground plane. Arc faults generate EMI [8], and the common-mode conductive interference (CMCI) part spreads all over the PV system through conductive media, such as power cables [22], which makes the PV power system a CMCI signal source. If a signal acquisition device is connected to the PV system and ground plane, the ground plane, stray capacitance, PV system, and signal acquisition device compose a flow path of CMCI, as shown in Fig. 1. The signal acquisition device will receive voltage signal when CMCI passes through the device, that is, the CMCV signal. Because CMCI can enter the signal acquisition device through the signal wire, the CMCV signal can be collected without sensors.

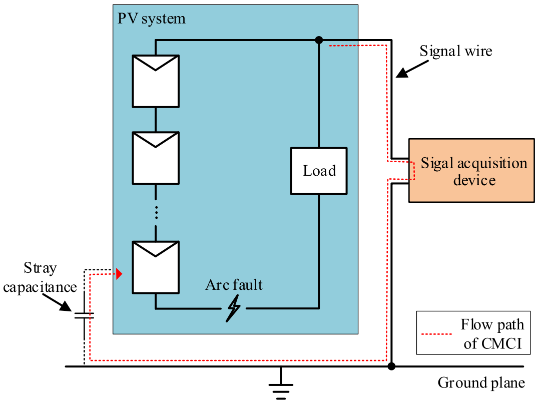

Fig. 1. Flow path of CMCI.

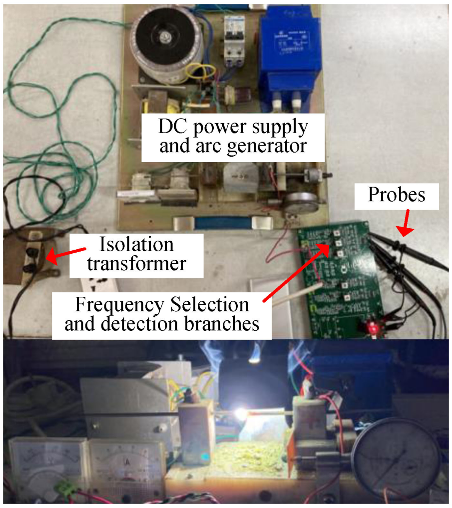

Fig. 2. Actual arc fault experimental platform.

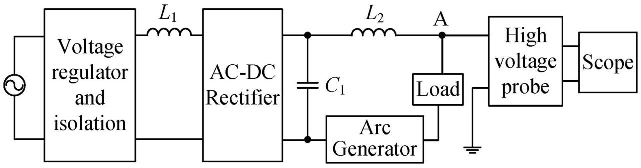

Fig. 3. Schematic of arc fault experimental platform.

B. *DC Series Arc Fault Experimental Platform*

To ensure that the repeatability of the test and tests are not influenced by environmental conditions, this article establishes a dc series arc fault experimental platform, as shown in Fig. 2, according to the UL1699B standard. Its schematic is shown in Fig. 3. The ac grid power source is isolated and rectified and then filtered by a capacitor C_1 and inductor L_2 connected to the arc generator. The load is a 10-Ω resistor that is used to simulate the attenuation of the CMCV signal caused by the resistance of

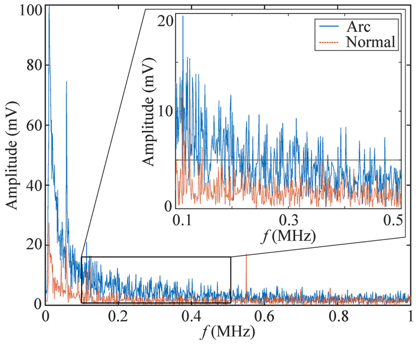

Fig. 4. Spectrum of original CMCV signal.

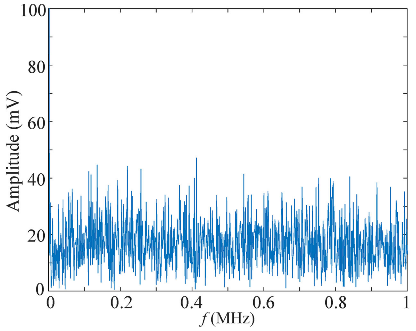

Fig. 5. Spectrum of white noise signal.

an actual PV power system. The high-voltage probe is used for high dc potential isolation, and the scope is for signal sampling. Point A is a sampling spot. Sampling is performed just after a stable arc is generated. According to the UL1699B standard, this article chooses tungsten–lanthanum alloy as the electrode material.

C. Characteristics of the CMCV Signal in the Time and Frequency Domains

First, this article used a scope and high-voltage probe to capture the original arcing CMCV signal at point A in Fig. 3. The probe is used to protect the oscilloscope from the damage of high potential to ground in the PV system, and the bandwidth of the probe is 100 MHz. Then, the spectrum was calculated, as shown in Fig. 4. As seen in the figure, the spectral range of the original CMCV signal is very wide and similar to the spectra of white noise, as shown in Fig. 5. Each frequency point has amplitude, and the amplitude is randomly varying, as shown in Fig. 6. In the normal situation, the amplitudes of some frequencies within 0–100 kHz are higher, revealing that the low-frequency noise exists in this band, and the source of noise could be the electronic instruments accessed to the power grid and power line interference. In the band of 100–500 kHz, each spectrum line of the arc situation is higher than the spectrum line of the normal situation. Additionally, the most important feature of the spectrum of the arcing CMCV signal is the randomly varying amplitude of each frequency component of the arcing CMCV signal, as shown in Fig. 6. This feature can be used as the breakthrough point of dc series arc fault detection.

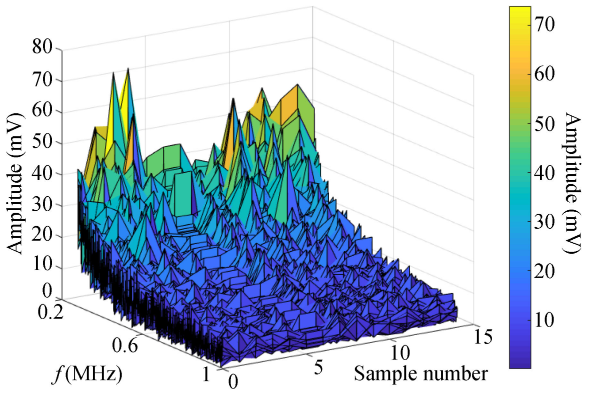

Fig. 6. Spectra of CMCV signals sampled in different times. The amplitude of the same frequency in different samples is disparate, proves that the frequency component of CMCV signal in arc situation has random-varying amplitude characteristic.

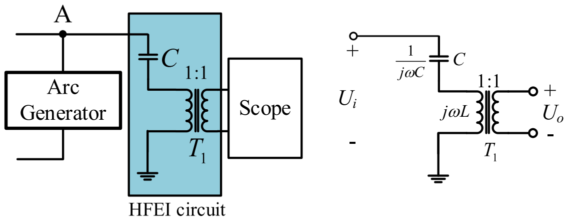

(a) (b)

Fig. 7. Schematic of HFEI sampling circuit and its equivalent circuit. (a) Schematic of HFEI circuit. (b) Equivalent circuit.

However, it is unsuitable to collect CMCV signals with high-voltage probes in practical arc fault detection devices (AFDDs) because this will increase the cost and the size of detection device, but it is necessary to isolate the high potential to protect the device from being disrupted by high voltage. Therefore, this article designed a high-frequency electromagnetic isolation (HFEI) sampling circuit composed of a capacitor C and a network transformer T_1, as shown in Fig. 7(a). The original CMCV signal is the input of the HFEI circuit, and the CMCV signal is the output of the HFEI circuit. The capacitance C is used to isolate the high dc voltage between the dc system and ground, and the network transformer T_1 is used for electrical isolation. The HFEI sampling circuit is a kind of series resonance circuit and has the effect of amplification; hence, it is conducive for signal processing. In terms of parameter selections of the capacitor and network transformer, it is reasonable to select the model of the network transformer first because the optional kinds of capacitances of the capacitor are more than the optional kinds of inductance of the network transformer. The only requirement for the parameter of the network transformer is a sufficiently wide band, for example, hundreds of kilohertz to dozens of megahertz. In this article, the model of the network transformer is HX1188NL, whose band is 100 kHz to 100 MHz. Then, the capacitance of the capacitor is chosen. Because the model of the network transformer has been determined, the principle of capacitor value selection is as follows: the amplified band is higher than 100 kHz, which is the low limit frequency of

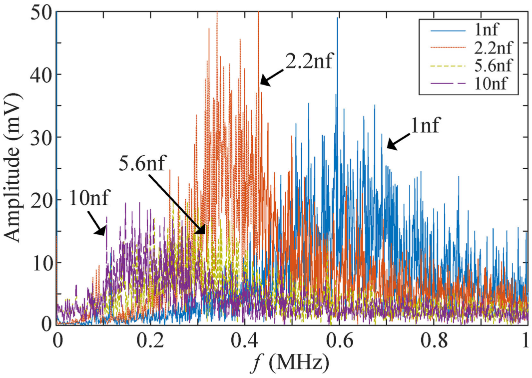

Fig. 8. Spectrum of output signal of HFEI circuit under different sampling capacitances.

HX1188NL and the best effect of amplification. The measured inductance value of HX1188NL is 79.7 μH, according to the formula of resonance frequency of the *LC* series resonance circuit

$$f = \frac{1}{2\pi\sqrt{LC}} \tag{1}$$

knows that the minimum capacitor value is 1.27 nF. Several capacitors were chosen, CMCV signals were collected under different capacitances, and the spectra were calculated. The spectra are shown in Fig. 8. As seen in Fig. 8, using a 2.2 nF capacitor can acquire the best amplification effect. A smaller capacitance has a higher impedance and causes much attenuation of the CMCV signal, and a larger capacitance will reduce the amplified band below 100 kHz. Therefore, this article chooses a 2.2 nF ceramic capacitor and network transformer HX1188NL to form an HFEI sampling circuit.

To obtain the characteristic band of the CMCV signal, it is necessary to analyze the amplitude–frequency response of the HFEI circuit. Because the output of the HFEI circuit is the inductor of the circuit, which is shown in Fig. 7(b), ignoring the equivalent series resistance of C and T_1, output U_o can be calculated as follows:

$$U_o = \frac{j\omega L}{j\omega L + {}^{1}\!/_{j\omega C}} U_i \overset{\omega=2\pi f}{=} \frac{4\pi^2 LCf^2}{1-4\pi^2 LCf^2} U_i \tag{2}$$

and U_o should reach its maximum value when the frequency of the input signal of the HFEI circuit equals the resonant frequency $f_0 = 1/2\pi\sqrt{LC}$. Under a 2.2 nF capacitor, the resonant frequency of the HFEI circuit is 380.08 kHz according to (1). As the spectrum of the original CMCV signal above 100 kHz is flat, the spectrum value of the CMCV signal, which is the output of the HFEI circuit, will reach a maximum at its theoretical maximum amplitude frequency point of 380 kHz because of the effect of resonant amplification of the HFEI circuit.

Then, the output signals of the HFEI circuit in the arc situation and normal situation were collected, and the spectra of the samples were calculated. The spectra are shown in Fig. 9. As seen in Fig. 9, the frequency of the maximum spectrum value of the CMCV signal is 380 kHz, and the experimental results correspond with the theoretical analysis. Regarding the spectrum characteristics of the arc CMCV signal, the spectrum amplitude of the CMCV signal in the arc fault situation is higher than that in the normal situation in the range of 0–1 MHz, especially at 300–500 kHz, which contains the theoretical maximum amplitude –frequency. The spectrum amplitude in the arc situation is ten times that in the normal situation. The test and analysis results indicate that it contributes to identifying arc faults if a 300–500 kHz frequency is chosen as the fault detection frequency. In the field of dc series arc fault detection, a common method of extracting the characteristic frequency band of arc fault current signals is collecting signals in actual arc fault experiments and then using FFT analysis or wavelet decomposition to process fault signals [2], [4], [10], [14], [20], [24]. The characteristic frequency of the arc current signal chosen by different researchers is not consistent; most of the chosen bands are in the range of 50–250 kHz, but the common ground of principle of the chosen characteristic frequency band in those studies is the band whose amplitude in fault situations is much higher than that in normal situations or the band that can avoid the noise frequency. Therefore, this article obeys the same principle, choosing the band whose amplitude in the fault situation is much higher than that in the normal situation 300–500 kHz as the characteristic frequency band of the arc fault CMCV signal.

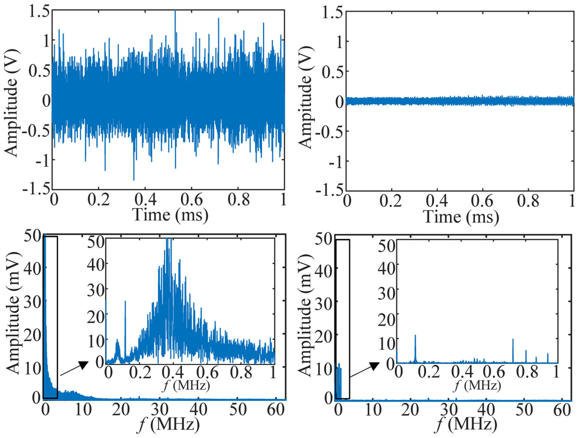

Fig. 9. Comparison of CMCV signals and spectra between arc and normal situation. (a) CMCV signal in arc situation. (b) CMCV signal in normal situation. (c) Spectrum in arc situation. (d) Spectrum in normal situation.

Previously, this article used tungsten–lanthanum alloy as the electrode material. However, the electrode material may influence the characteristics of the arcing CMCV signal; hence, tungsten–lanthanum electrodes were replaced by copper electrodes in the same specification. Then, an arc fault was generated under the same experimental conditions, and dozens of signal samples of output of the HFEI circuit were collected. After that, the average spectrum under the copper electrode was calculated and compared with the average spectrum under tungsten–lanthanum electrodes. The comparison results are shown in Fig. 10. As seen in the figure, their frequency spectra are almost identical, especially in the characteristic frequency band of 300–500 kHz, proving that the electrode material has

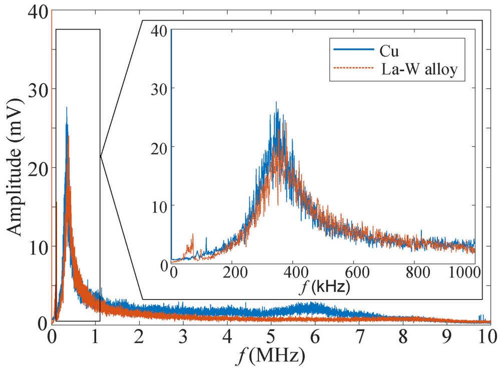

Fig. 10. Average spectra of output of HFEI circuit in arc situation under different electrode materials.

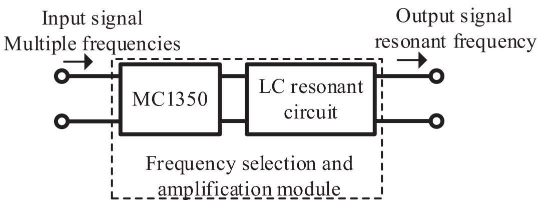

Fig. 11. Structure of FSA module.

little effect on the spectrum of the arcing CMCV signal. Subsequent experiments were continued with lanthanum–tungsten alloy electrodes.

III. DESIGN OF MULTIPLE FREQUENCY SELECTION AND DETECTION BRANCHES AND FAULT FEATURE QUANTITY EXTRACTION

A. *Multiple Frequency Selection and Detection Branches*

In the field of dc series arc fault detection, researchers usually use wavelet decomposition to extract the characteristic frequency bands of arc current, but this kind of approach requires high-performance hardware, such as a fast CPU, high-speed data acquisition board, and large memory space. This leads to high costs. This article used a simple *LC* parallel resonance circuit to extract feature frequency components and rapidly reduce the hardware performance requirements. Because the amplitude of each component of the CMCV signal is very weak, this article connected the resonant gain chip MC1350 to the *LC* circuit to amplify the component. The chip and the *LC* circuit compose the frequency selection and amplification (FSA) module, as shown in Fig. 11. The selective frequency of the module can be changed by adjusting the parameters *L* and *C*. After measuring, the half-power bandwidth of the FSA module is approximately 20 kHz, as shown in Fig. 12. In the figure, the gain is normalized, that is, the gain at the selective frequency is 1.

According to the spectral analysis of CMCV signals, the frequency of the module's output is still high, more than 100 kHz. The load of the A/D converter is heavy if the sampling frequency meets the requirements of Shannon's sampling theorem. However, after several experiments, it was found in this article that the magnitude of a single frequency component has randomly varying characteristics because of the randomness of arc discharging. The waveform of the frequency component has an envelope line, as shown in Fig. 13. This is similar to the amplitude modulation (AM) signature defined in radio engineering. The AM signal is composed of two parts: a high-frequency variable amplitude signal and low-frequency envelope lines. The high-frequency variable amplitude signal is called the "carrier wave," and the low-frequency envelope lines are called the "modulating wave." The AM signal also belongs to the amplitude variation signal, and the modulating wave is caused by the phenomenon of amplitude variation of the carrier wave. If the amplitude of the carrier wave is constant, there will be no modulating wave. The process of extracting the modulating wave from the carrier wave is called "demodulation." In fact, demodulation is the process of frequency reduction that transfers a high-frequency signal to a low-frequency signal. If the component and the envelope can be treated as carrier waves and modulating waves, it is possible to realize frequency reduction. Unlike [23], Fenz et al. used a modulator to achieve frequency transformation directly; this article connected a simple diode detector to the FSA module. The diode detector demodulates a low-frequency upper envelope signal from the frequency component to perform frequency reduction, and the output of the diode detector is the upper envelope line of the frequency component. The structure of the diode signal detector is shown in Fig. 14. Here, the precise amplitude–frequency information cannot be acquired after the frequency component goes through the diode detector; however, the most important feature of the spectrum of the arcing CMCV signal is that the amplitude of each frequency component of the

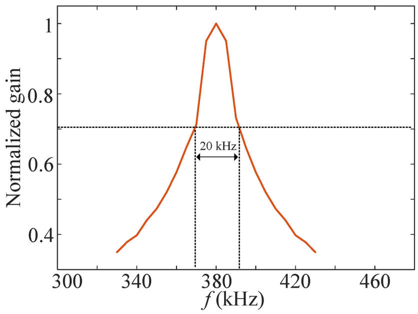

Fig. 12. Amplitude–frequency characteristics of FSA module.

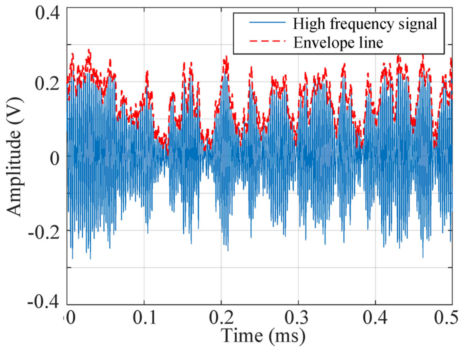

Fig. 13. High-frequency arc signal component and its upper envelop line.

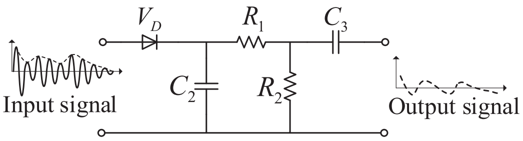

Fig. 14. Structure of diode detector.

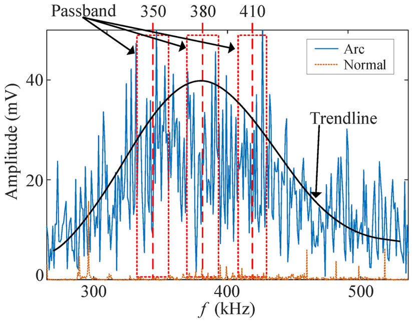

Fig. 15. Selective frequency allocation of FSA module of detection branch.

arcing CMCV signal is randomly varying according to the analysis of the CMCV signal in Section II-C, and the characteristic of the randomly varying amplitude, which means the component is similar to the AM signal, is exactly what the diode detector handles. The diode detector can extract the most important feature from the frequency components of arcing the CMCV signal. Therefore, it is not necessary to accurately reproduce the amplitude–frequency information of the component of the CMCV signal.

The frequency of the FSA module should be chosen from the range 300–500 kHz, which is the characteristic band of the CMCV signal. Several frequency selection–detection branches can be applied to avoid misjudgment when a single frequency point is disturbed, and there should be at least a 20 kHz frequency gap between each pair of branches' central frequencies. As seen in Fig. 9, in the arc situation, the amplitude of 380 kHz is the overall highest; hence, the resonance frequency of the FSA module of the detection branch is allocated from 380 kHz. In addition, considering that the half-power bandwidth of the FSA modules designed in this article is 20 kHz; if f is the selective frequency of the FSA module, the covering frequency range is $[f-10\text{ kHz}, f+10\text{ kHz}]$. Therefore, up to ten FSA modules can be applied in the range of the characteristic band. To avoid overlapping passbands, this article allocates the selective frequency of FSA modules at intervals of 30 kHz, which is 1.5 times the half-power bandwidth. Finally, the central frequencies of the FSA modules of the three detection branches are set at 350 kHz, 380 kHz, and 410 kHz, as shown in Fig. 15. More branches mean wider frequency coverage and higher detection reliability under outer interference, but the cost will increase. The reason for choosing three detection branches is explained in Section V-D. The AFDD can be formed by connecting the input terminals of the three detection branches with the output terminals of the HFEI circuit and the output terminals of the three detection branches with the three input terminals of the data processing unit. The structure of the device is shown in Fig. 16. If more branches are added, the principle of 1.5 times the half-power bandwidth should be obeyed, that is, the selective frequency interval between existing branches and branches to be added is 1.5 times the half-power bandwidth. After measuring, the amplitude–frequency curve of each FSA module is shown in Fig. 17. As seen in the figure, the half-power bandwidths of the three FSA modules are all approximately 20 kHz.

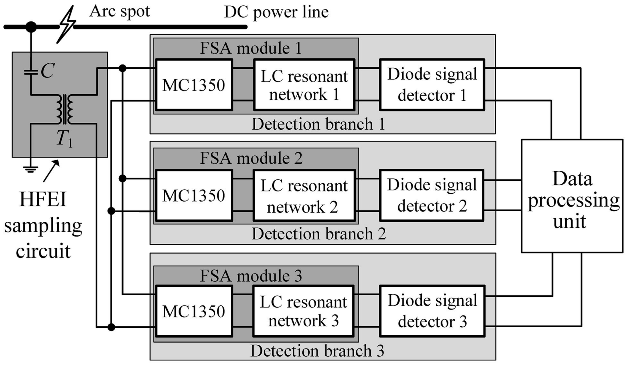

Fig. 16. Structure of the detection device for the CMCV signal.

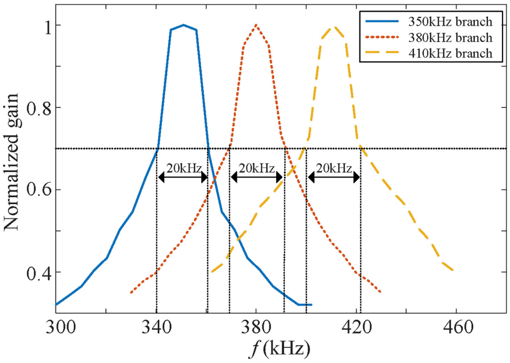

Fig. 17. Amplitude–frequency curves of FSA modules of three detection branches.

B. Extraction of Feature Quantities in the Time and Frequency Domains

1) Waveform and Spectrum of the Output Signal of Detection Branches: The output signal of each detection branch is collected in arc and normal cases, and their spectra are calculated, as shown in Figs. 18 –20. CndVarc1, CndVarc2, and CndVarc3 are the outputs of detection branch 1, detection branch 2, and detection branch 3 in the arc fault situation. As seen in the figures, the waveforms of CndVarc1, CndVarc2, and CndVarc3 are very similar. The reason for this phenomenon is the randomly varying amplitude characteristic of all frequency components of the CMCV signal in the arc fault situation, which has been proven by Fig. 6. A similar changing pattern of amplitude of frequency components causes similar envelope lines, and the output of the detection branch is the upper envelope line of the frequency component; hence, the outputs of detection branches in arc situations are similar. However, the difference between CndVarc and Vnormal is significant, which means that the outputs of the

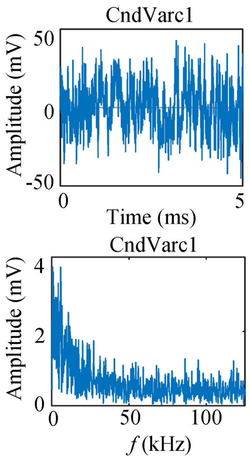

Fig. 18. Comparison of the signal and spectrum of the 350 kHz detection branch output between arc and normal situations.

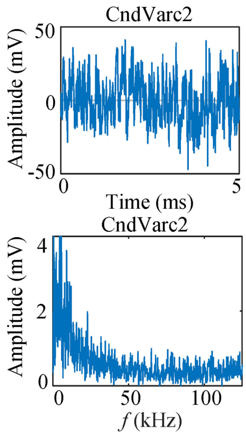

Fig. 19. Comparison of the signal and spectrum of the 380 kHz detection branch output between arc and normal situations.

three detection branches will be discrepant at the same time between the arc fault situation and normal situation. When a device is disturbed by an interference signal, it is difficult for the interference signal to influence all three detection branches because the bandwidth of the interference signal is normally limited. This simultaneity feature can be used to identify the arc fault. Focusing on the output difference between the arc fault situation and normal situation, compared with the normal situation, the outputs of the detection branches in the arc situation fluctuate violently in the time domain; in other words, the dispersion of the detection branches' output in the arc case is larger than normal. In the spectral aspect, the amplitude–frequency of the full band increased greatly when an arc occurred. This means that the spectral energy of each branch's output increases when an arc fault occurs. Moreover, the high amplitude–frequency band of the detection branch's output is concentrated at 0–20 kHz, which means that the sampling frequency can be lowered to 40 kHz. Therefore, inexpensive hardware, such as MCS 51, can be applied to this detection device. The spectrum amplitude of higher than 100 kHz is similar to that of 50–100 kHz; hence, this article focuses on the spectrum of 0–100 kHz.

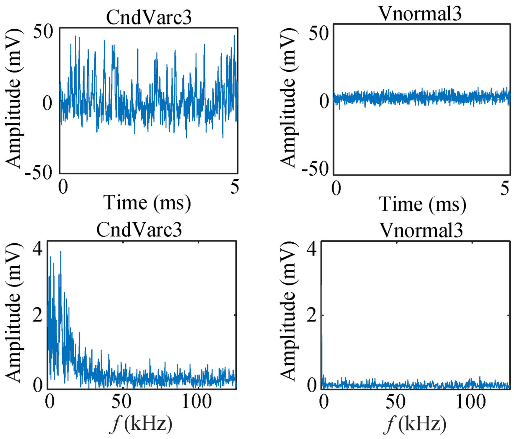

Fig. 20. Comparison of the signal and spectrum of the 410 kHz detection branch output between arc and normal situations.

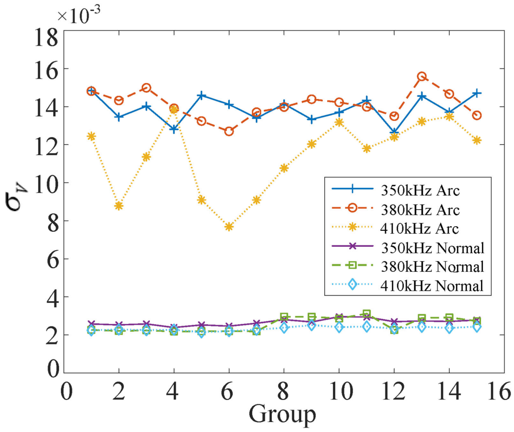

Fig. 21. STD values of the detection branch outputs in arc and normal situations.

2) Quantity Extraction in the Time Domain: In the signal analysis of the detection branch outputs, the dispersion of the output in the arc situation is much larger than that in the normal situation. Therefore, this article uses the sample standard deviation (STD) to describe this dispersion. The calculation formula of the STD is

$$\sigma = \sqrt{\frac{1}{N-1}\sum_{i=1}^{N}\left|x\left(i\right)-\bar{x}\right|^{2}} \tag{3}$$

where $x(i), i = 1, 2, \ldots, N$ is the sample group to be calculated and $\bar{x}$ is the mean value of the sample group. σ_V is used to denote the STD.

The STDs of the detection branch outputs in the arc and normal situations are computed, as shown in Fig. 21. As seen in the figure, the STDs of all detection branch outputs fluctuate rapidly, and the STDs in the arc situation are at least two times those in the normal situation. This proves that the STD value can effectively distinguish the outputs of the branches in the arc situation. Therefore, this article chooses the STD as the time-domain feature quantity of the detection branch's output.

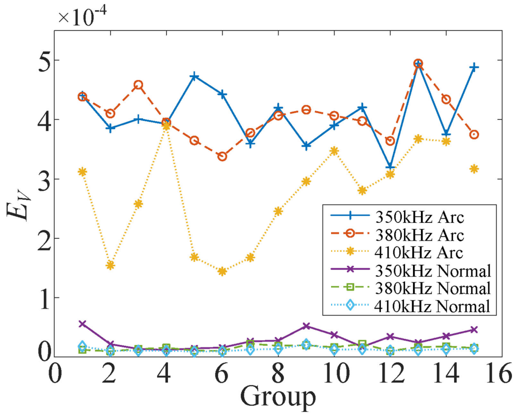

Fig. 22. Spectral energy of the detection branch outputs in arc and normal situations.

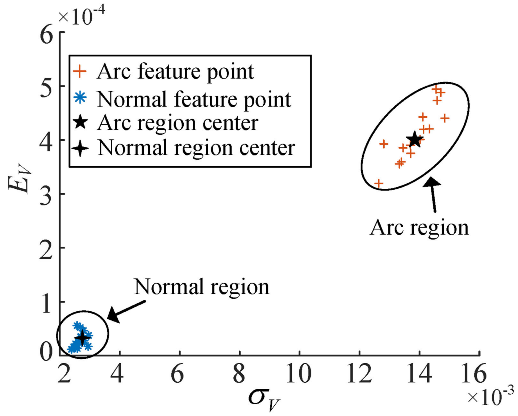

Fig. 23. Division of the arc and normal regions and settings of the central coordinates of 350 kHz detection branch.

3) Quantity Extraction in the Frequency Domain: In the spectral analysis of the detection branch outputs, the energy of the spectrum will increase when an arc fault occurs. Therefore, the value of spectral energy is defined as follows:

$$E = \sum |A(f)|^2 \tag{4}$$

where $A(f)$ is the magnitude–frequency parameter of the branch output after Fourier transform.

The arc and normal spectral energy (E_V) of the three detection branch outputs is computed, as shown in Fig. 22. As seen in the figure, the spectral energy of all branch outputs in the arc situation is much larger than those in the normal situation. Therefore, this article chooses spectral energy as the feature quantity of the frequency domain.

IV. SIMILARITY CRITERION BASED ON THE EUCLIDEAN DISTANCE AND ARC FAULT DIAGNOSIS ALGORITHM

A. Construction of the STD-Energy Feature Plane

The 2-D fault feature plane, called the $\sigma - E$ plane, is composed of the STD σ and spectral energy E. The two feature quantities are used to form the feature coordinates of the branch outputs, (σ, E). Taking the 350 kHz detection branch as an example, the feature coordinates of the branch output are plotted, as shown in Fig. 23. As seen in Fig. 23, in a normal situation, the feature coordinates of the branch output cluster in the bottom-left area of the plane and the coordinates of the branch output cluster in the upper-right area in the arc situation. Therefore, the $\sigma - E$ plane can be split into three regions: the arc region, the normal region, and the disturbed region. It is necessary to set the region's central coordinate because of the randomness of the arc CMCV signal. This article uses the mean value of 15 arc groups of STD features, denoted by $\bar{\sigma}_{V1}$, and the mean value of 15 arc groups of spectral energy features, denoted by $\bar{E}_{V1}$, to build up the central coordinate of the arc region, denoted by $(\bar{\sigma}_{V1}, \bar{E}_{V1})$. The central coordinates of the normal region, denoted by $(\bar{\sigma}_{NV1}, \bar{E}_{NV1})$, are set in the same way. In Fig. 23, the centers of the arc and normal regions are marked by a pentagram and a four-pointed star, respectively, and are denoted similarly hereafter.

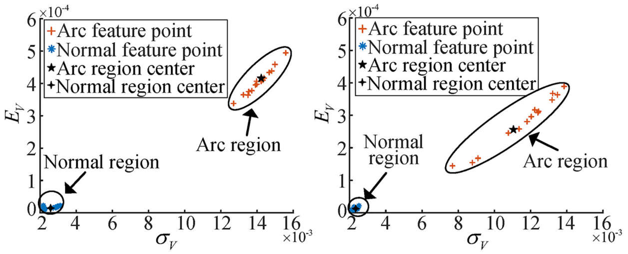

Fig. 24. Spectral energy of the detection branches outputs in arc and normal situations. (a) 380 kHz detection branch. (b) 410 kHz detection branch.

The feature quantities of the 380 and 410 kHz detection branch outputs are the same, as shown in Fig. 24.

B. Similarity Criterion and Arc Fault Detection Algorithm

To confirm in which region the 2-D feature coordinate of a sample is located, this article uses the Euclidean distance to measure the distance to the region's center. Assuming there are two coordinates, $(x_1, y_1), (x_2, y_2)$, the Euclidean distance between them is defined as follows:

$$d = \sqrt{(x_1 - x_2)^2 + (y_1 - y_2)^2}. \tag{5}$$

Assuming the feature coordinate of one sample is $C(\sigma_1, E_1)$, the central coordinates of the arc and normal regions are $A(\sigma_A, E_A)$ and $N(\sigma_N, E_N)$, respectively. The distance between $C(\sigma_1, E_1)$ and $A(\sigma_A, E_A)$, called the arc center distance d_A, is defined as follows:

$$d_A = \sqrt{(\sigma_1 - \sigma_A)^2 + (E_1 - E_A)^2} \tag{6}$$

and the distance between $C(\sigma_1, E_1)$ and $N(\sigma_N, E_N)$, called the normal center distance d_N, is defined as follows:

$$d_N = \sqrt{(\sigma_1 - \sigma_N)^2 + (E_1 - E_N)^2}. \tag{7}$$

$C(\sigma_1, E_1)$ should be close to the center of the arc region if this sample is captured when an arc fault occurs; therefore, the inequation $d_A \ll d_N$ will be satisfied. If this sample is collected when the dc system is normal, $C(\sigma_1, E_1)$ should be near the

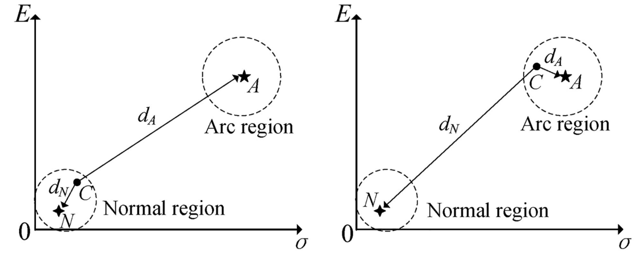

Fig. 25. Geometric position relationships in two situations. (a) C is a normal sample. (b) C is an arcing sample.

center of the normal region, and the inequation $d_A \ll d_N$ will be satisfied. Fig. 25 shows the geometric relationships in these two situations.

Based on this fact, this article constructs a kind of similarity criterion, which can be calculated as follows:

$$P_A = 1 - \frac{d_A}{d_A + d_N}$$

$$P_N = 1 - \frac{d_N}{d_A + d_N} \tag{8}$$

where P_A is the similarity parameter of the arc and the interval is (0,1). An arc fault probably occurs if P_A is close to 1; P_N is the similarity parameter of the normal situation, and the system is normal if P_N tends toward 1. It should be noted that equation $P_A + P_N = 1$ is always satisfied.

A simple arc fault detection algorithm is designed in this article, as shown in Fig. 26. Since the region of the arc is relatively large compared with the normal region, according to Figs. 23 and 24, this article sets the threshold values of the arc and normal situations to 0.6 and 0.9, respectively, to increase the diagnostic accuracy. The algorithm will determine that the detection device is disturbed if neither similarity parameter can reach its threshold because there are only two kinds of situations (arc and normal) for arc fault detection in the dc power system. Second, sampling and judgment will be executed in this situation. Because the amplitudes of the frequency points of the CMCV signal increase rapidly at arc occurrence, the feature coordinates of all detection branch outputs should be located in their arc regions. If not, the algorithm should not give an arc alarm. However, the detection algorithm should not give an arc fault alarm when the dc switch is operating because the dc switch can generate a kind of flash arc. Therefore, the algorithm will wait for a period of time for a second detection after an arc fault is detected. The algorithm will give an arc fault alarm if an arc fault is detected a second time. This article sets the waiting time value to 0.2 s.

V. VALIDATION OF ARC FAULT DETECTION METHOD

A. Verification of Arc Fault Detection Accuracy

First, the learning and setting sample acquisition experiment was performed. There were two groups in this experiment: the arc fault group and the normal group. The only difference between the two groups was whether the electrodes were pulled apart. In each group, we collected 15 signal samples of the HFEI circuit output and 15 signal samples of the detection branch output. The former were used as learning samples for the intelligent algorithm, and the latter were used as setting samples for the proposed algorithm. Because the accuracy of classical intelligent arc fault detection algorithms, such as neural networks and support vector machines (SVMs), is dependent on the number of learning samples, this article reduced the number of learning or setting samples to compare the detection accuracy of the proposed method with that of the classical intelligent fault detection algorithm. Then, each group would capture 100 test samples in arc and normal situations again for arc fault detection. In terms of the common intelligent arc fault detection method, this article introduced feature extraction, which was based on wavelet decomposition combined with an intelligent identification algorithm, for comparison with the method proposed in this article. However, many researchers have made different choices in the field of selection regarding the parameters of wavelet decomposition and fault detection algorithms, and there is no universally accepted choice that has the best effect. Therefore, this article selected two kinds of classical arc fault detection methods, wavelet-SVM and wavelet-forward feedback neural network (FFNN), as comparative objects of accuracy; the former was representative of the classification algorithm, and the latter was representative of the neural network. The learning parameters of the two kinds of intelligent algorithms were default values of relevant software toolboxes. In terms of learning and setting sample acquisition, the learning and setting samples used by the three detection methods were obtained at the same time; that is, the samples used by wavelet-SVM and wavelet-FFNN were the output signals of the HFEI circuit, and the samples used by the proposed method were the outputs of the detection branches. The acquisition process of the learning and setting samples is shown in Fig. 27. After sample acquisition, the process of fault detection begins. First, setting samples were used to set the central coordinates of arc and normal regions. Then, the fault detection algorithm, as shown in Fig. 26, was run. The result of the similarity calculation and threshold value space is shown in Fig. 28, and the accuracy statistic of arc detection is shown in Table I. As seen in Fig. 28, the 3-D similarity values of arc and normal samples are in the corresponding space except for only seven 3-D similarity values of an arcing sample. This reveals that the accuracy of the proposed method is great. Then, two classical methods were used for fault diagnosis of samples waiting for fault diagnosis, and their accuracy values were counted and compared with that of the proposed method. The comparison results are shown in Table II. In the table, the malfunction rate is the ratio of the number of wrong actions to the total number of judgments, and the rejection rate is the ratio of the number of failures to actuate in the fault situation

TABLE I
STATISTIC OF ARC DETECTION

Sample number	Event type	Number of correct detections	Accuracy
1~100	Arc faults event	93	93%
101~200	Normal event	99	99%

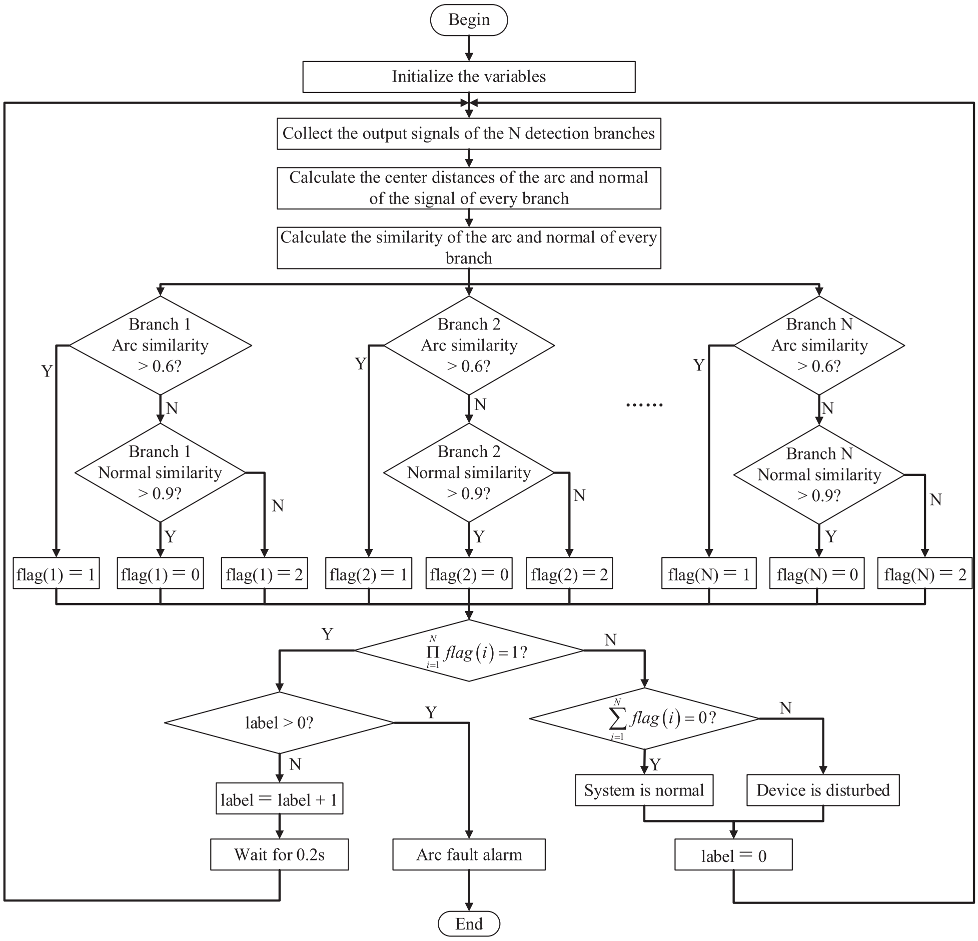

Fig. 26. Arc fault judgment algorithm for multiple detection branches.

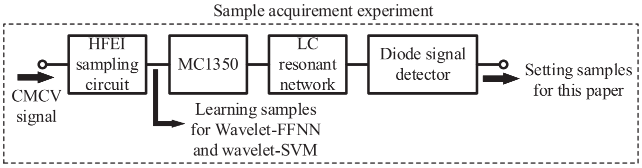

Fig. 27. Acquisition process of learning and setting samples.

TABLE II
COMPARISON OF THE EFFECT OF THE THREE SCHEMES

Method	Number of samples	Malfunction rate	Rejection rate	Judgment accuracy
Wavelet-FFNN	30 samples to train, 200 samples to test	2%	16%	91%
Wavelet-SVM	30 samples to train, 200 samples to test	2%	8%	95%
This article	30 samples to set, 200 samples to test	1%	7%	96%

to the total number of judgments. As seen in Table II, under the same allocation of samples, the detection method proposed in this article has a low rejection and malfunction rate, which maintains the same judgment accuracy as wavelet-SVM. In the case of fewer training samples, the FFNN has a higher rejection rate and lower overall judgment accuracy. Compared with neural network identification, the arc detection method proposed in this article maintains high accuracy with fewer samples.

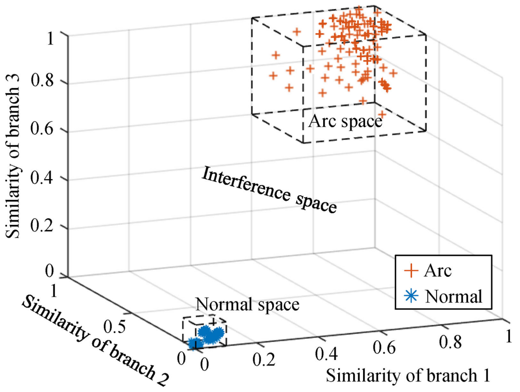

Fig. 28. Result of the 3-D similarity values and threshold value space.

B. Speed and DC Switch Operating Malfunction Test

According to the UL1699B standard, the AFDD must extinguish the arc within a specific time after arc fault occurrence. This specific time is relevant to the arc current, for example, 2 s under 7 A and 0.8 s under 14 A, but the time should not exceed 2.5 s. Therefore, the detection speed of the AFDD must meet the

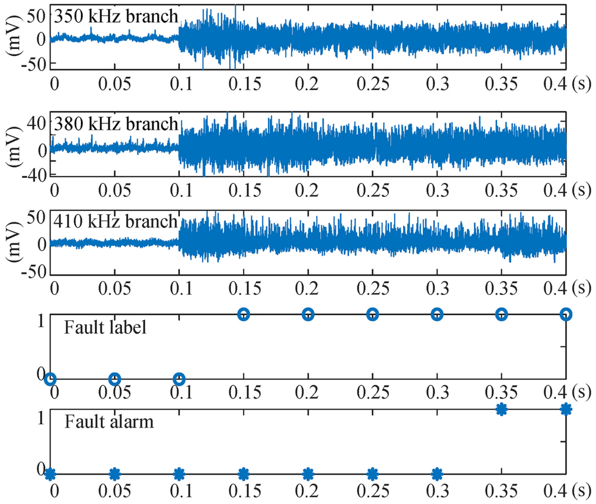

Fig. 29. Speed test of the algorithm.

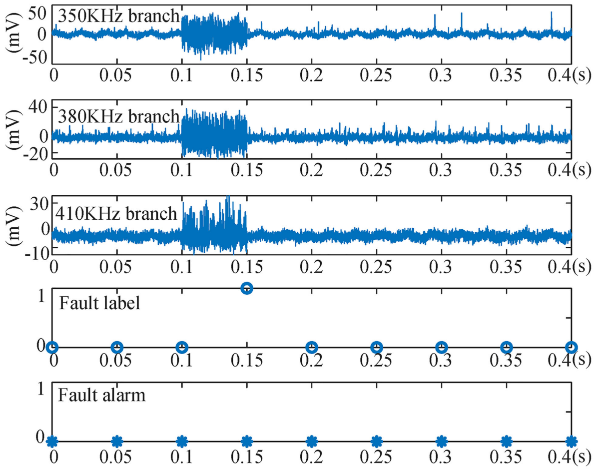

Fig. 30. Algorithm misoperation test when the dc switch is operating.

standard requirements. To this end, the actuation time of the arc fault detection method was measured. A continuous arc fault was made at 0.1 s, and the action time of the algorithm was observed. The results are shown in Fig. 29. The algorithm detects the fault and sets the fault label to 1 at 0.05 s after the arc fault occurrence because sampling 2000 data points at 40 kHz requires 0.05 s. The algorithm sets the fault alarm to 1 at 0.35 s after waiting for 0.2 s for two arc fault confirmations. It takes 0.25 s from fault occurrence to the alarm, proving that the detection speed of the method is able to meet the requirement of the UL1699B standard.

Additionally, a flash arc was generated to simulate the arc produced by the dc switch operation. The AFDD should not operate in this situation. The test results are shown in Fig. 30. The algorithm detects an arc fault in the sample that is collected during the interval 0.1–0.15 s, and the fault label is set to 1, but no arc fault is detected in any subsequent samples, and the algorithm sets the label to 0. The algorithm successfully ignores the dc switch operation arc, and there is no fault alarm during the whole process.

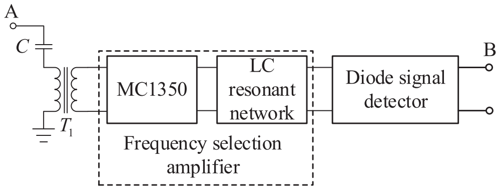

Fig. 31. Location of input and output terminals of frequency selection and detection branch. A is the input terminal, and B is the output terminal.

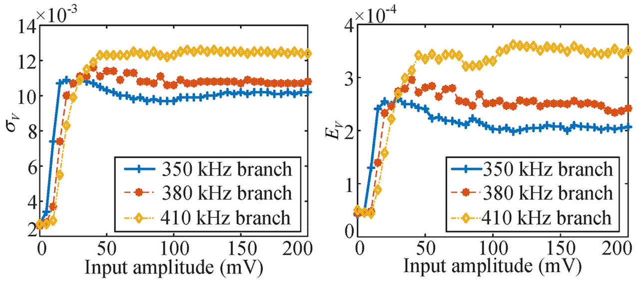

Fig. 32. Input–output characteristics of detection branches. (a) STD-input. (b) Spectral energy-input.

C. Discussion of the Universality of the Central Coordinate Settings

The key to the accuracy of the detection method that this article proposes is the setting of the region's central coordinates. Hence, this article studied the relationships between the two feature quantities of the detection branch outputs and the magnitude of the input signal of the HFEI circuit. To precisely control the magnitude of the input of the HFEI circuit, which is point A of Fig. 31, a signal generator generated a white noise signal whose spectral characteristics are similar to those of the arc CMCV signal to replace the CMCV signal. To describe the relationship between the STD feature, spectral energy feature, and amplitude of input white noise, for each detection branch, 41 output signal samples were used, and each sample contained 2000 data points. The two features of the branch outputs that were sampled at point B of Fig. 31 were calculated at different input levels, as shown in Fig. 32. Because the white noise characteristics and CMCV signal are not completely consistent, the feature quantities of the detection branch outputs when the input is white noise may not be completely consistent with those when the input is the CMCV signal, but to some extent, this can show the input–output characteristics of the detection branches. As seen in Fig. 32, the two feature quantities of all detection branch outputs increase quickly and remain in a stable range when the magnitude of the input increases to approximately 30 mV. Therefore, the detection branches designed in this article have a “0–1” input–output characteristic; that is, the two feature quantities of the output of the detection branch are always in the determined range regardless of the amplitude of white noise. Therefore, if the input of the detection branch is the CMCV signal, the branch will also have a “0–1” input–output characteristic because the spectral characteristics of the CMCV signal are similar to white noise, and the detection branches also have high sensitivity. Hence, the values of the central coordinates of regions set in the dc arc fault

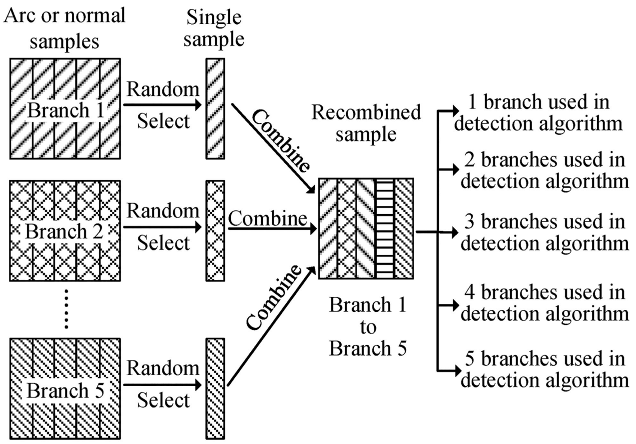

Fig. 33. Selection–recombination process.

experiments can be applied to actual dc power systems directly; in other words, the values of the central coordinates of regions set in the dc arc fault experiments can be treated as default values, using default values for the first time run of the detection device. In this way, the actual arc fault data do not need to set the central coordinates of arc regions.

D. Influence of Branch Amount on Detection Reliability

The number of detection branches could influence the reliability of fault detection accuracy since the detection band coverage is determined by the number of detection branches. This article has verified the relationship between the number of detection branches and detection reliability. Two more detection branches were added, and their frequencies were 320 and 440 kHz. Together with the existing three detection branches, the band of 320–440 kHz was covered. When the characteristic frequency band is disturbed, the interference will make the output of the detection branch of the corresponding frequency band similar to the arc situation, while the output of other branches is still normal, but it is inconvenient to add interference during experiments. However, the bandwidth of external interference is generally narrow, and the interference will only increase the amplitudes of some frequencies rather than the whole characteristic band, whose frequency range is wider than the interference. Therefore, the interference will cause the output of the detection branch whose frequency band covers the interference to be more similar to the output in the arc situation, and other branches maintain normal outputs. Therefore, this article conducted an equivalent approach called the "selection–recombination process." First, one subsample was selected randomly from the sample database of each detection branch and then combined in order of branch number to form a recombined sample. The selection–recombination process is shown in Fig. 33. Due to random selection, it is inevitable that samples selected from the sample database of some branches belong to the arc situation and samples selected from the database of other branches belong to the normal situation. In this way, the situation of interference could be simulated. In this section, 1000 recombined samples were acquired after 1000 selection–recombination processes were performed. Meanwhile, the running arc fault detection algorithm is shown in Fig. 26, with different numbers of detection branches, counting the correct identification times, and setting the ratio of correct identification times to total identification times as detection reliability. The box plot of reliability versus the number of detection branches is shown in Fig. 34. As seen in the figure, the increasing speed of detection reliability slows down as the number of detection branches increases. In addition, a greater number of branches means a higher cost. Considering cost and reliability, it is more appropriate to apply three detection branches.

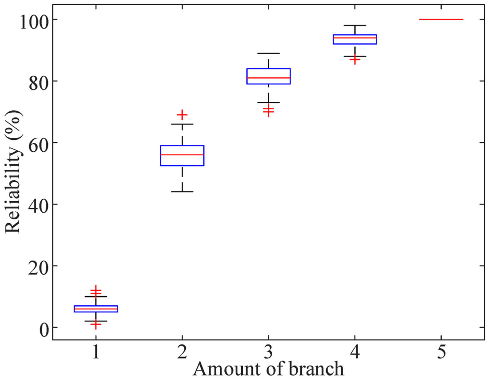

Fig. 34. Box plot of detection reliability verses number of detection branches.

E. Discussion About Anti-Interference Ability

The operation of various power electronics' devices in power systems introduces high-frequency noise into voltage and current. The spectrum of noise concentrates at the switching frequency and its multiples and reaches the maximum amplitude at the switching frequency. AFDD may have an incorrect action if the noise band overlaps the frequency band of the current used in arc fault detection. Seo et al. [24] emphatically discussed the influence of the noise of the switching power supply on AFDD. This research used current as the detection object. The strong noise of an LED driver, which is a type of switching power supply, is dominant in the 20–40 kHz and 60–80 kHz fault detection bands. The amplitude of noise was much higher than the amplitude of the arc current at the switching frequency, and AFDD was confused in this situation. Therefore, researchers believe that AFDD should avoid the noise frequency range in determining the presence of arcing, and the reliability would be better if AFDD could avoid or eliminate the influence of interference. In terms of the switching frequency of power electronic devices, the general distributed PV inverter is less than 20 kHz and that of the common switching power supply is 50–130 kHz. However, the characteristic frequency band of the arcing CMCV signal is 300–500 kHz, avoiding the band of electronic noise. Therefore, the interference of the power electronic device will not greatly affect the arc fault diagnosis method proposed in this article.

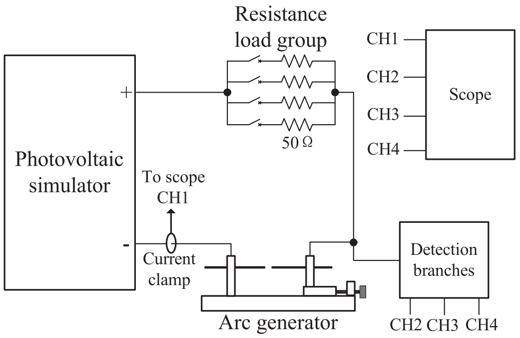

Fig. 35. Schematic of PV power system experimental platform.

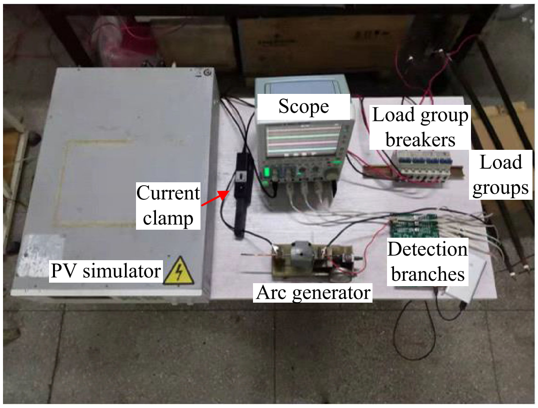

Fig. 36. PV power system experimental platform.

TABLE III
PARAMETERS OF PV MODULE

$U_{oc}(V)$	$I_{sc}(A)$	$U_m(V)$	$I_m(A)$
37.4	8.8	29.5	8.14

F. Influence of Load or Irradiation Changes on the Effectiveness of the Proposed Method

To research the influence of load or irradiation changes, which is a common phenomenon in actual PV power systems, on the proposed detection method, this article established a PV power system, as shown in Fig. 35, and the corresponding photograph is shown in Fig. 36. A Chroma 62150H-1000S PV simulator was used to simulate a PV string cascaded by four PV modules whose parameters are shown in Table III. The loads of the PV series were composed of four 50-Ω resistance loads in parallel, and each resistance load can be independently connected to or removed from the power system with dc circuit breakers to simulate load changes. An arc generator was connected to the system in series and pulling the electrode part can create a series arc fault. The current clamp was used for current monitoring and load change confirmation, and the method proposed in this article does not use current for arc fault detection.

In this section, three groups of experiments were designed. In the first group, the four loads were cut off or connected randomly after the arc was ignited. Meanwhile, the current and outputs of the three detection branches were captured. Then, the algorithm proposed in this article was used to identify arc faults. The purpose of this group of experiments was to verify whether the load change influences the effect of the proposed detection method. The results are shown in Figs. 37 and 38. As seen in the figures, during arc burning, regardless of how the load changes, the outputs of the three detection branches are relatively stable and twice the normal situation, and the detection algorithm continuously gives a fault alarm. The results prove that the load change under arc situations will not influence the detection branches and algorithm, and the method proposed in this article still maintains effectiveness and accuracy.

The second group of experiments repeated all steps of the first group but in a normal situation. The purpose of this group of experiments was to verify whether load change confuses the proposed detection method and causes incorrect action. The results are shown in Figs. 39 and 40. As seen in the figures, no matter how the load changes, the outputs of the three detection branches remain low, and the algorithm does not give fault alarms. Only arc faults can trigger the branches and algorithm. The results reveal that the load change under a normal situation will not cause misjudgment of the proposed method.

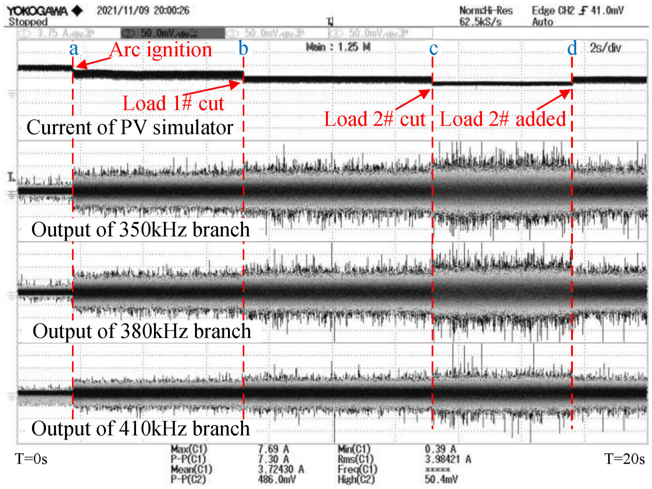

Fig. 37. Influence of load change during arc fault on the outputs of three detection branches.

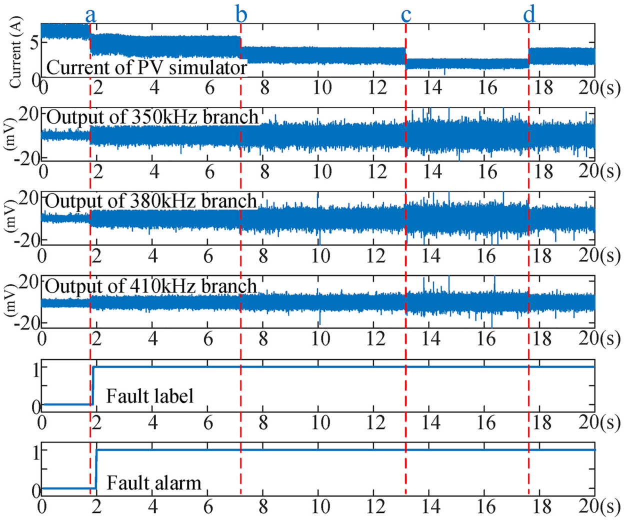

Fig. 38. Influence of load change during arc fault on detection algorithm.

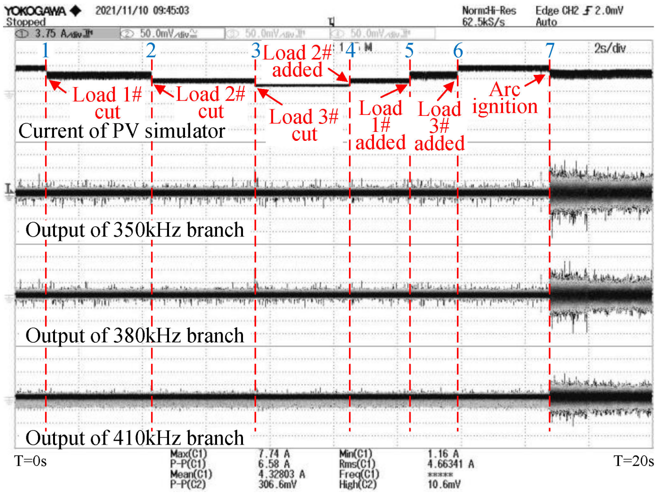

Fig. 39. Influence of load change on outputs of three detection branches in normal situation.

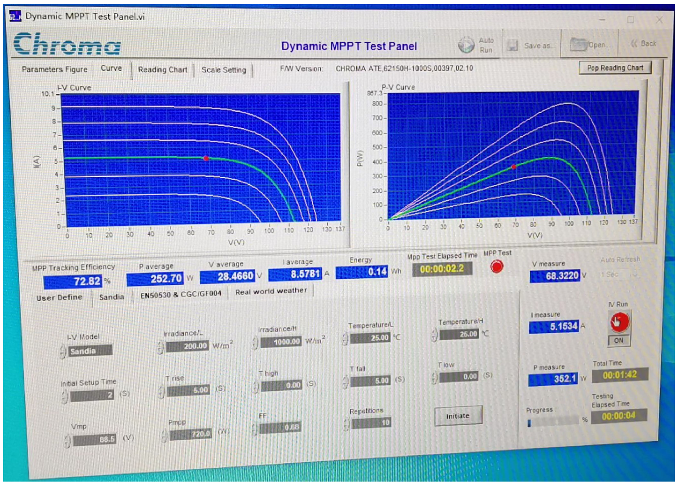

F/W Version: CHROMA ATE,62150H-1000S,00397,02.10

MPP Tracking Efficiency 72.82 %
P average 252.70 W
V average 28.4660 V
I average 8.5781 A
Energy 0.14 Wh
Mpp Test Elapsed Time 00:00:02.2
MPP Test
V measure 68.3220 V
Auto Refresh 1 Sec

User Define | Sandia | EN50530 & CGC/GF004 | Real world weather

I-V Model Sandia
Irradiance/L 200.00 W/m²
Irradiance/H 1000.00 W/m²
Temperature/L 25.00 °C
Temperature/H 25.00 °C
Initial Setup Time 2 (S)
T rise 5.00 (S)
T high 0.00 (S)
T fall 5.00 (S)
T low 0.00 (S)
Vmp 88.5 (V)
Pmpp 720.0 (W)
FF 0.68
Repetitions 10
Initiate
I measure 5.1534 A
IV Run ON
P measure 352.1 W
Total Time 00:01:42
Progress %
Testing Elapsed Time 00:00:04

Fig. 41. Setting interface of simulation of irradiation change.

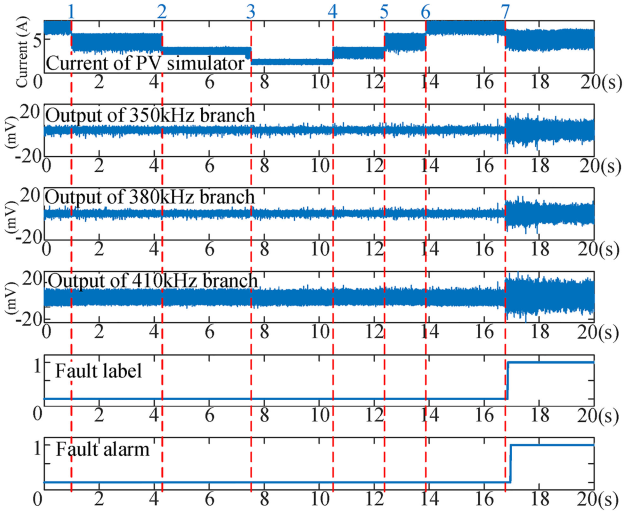

Fig. 40. Influence of load change on detection algorithm in normal situation.

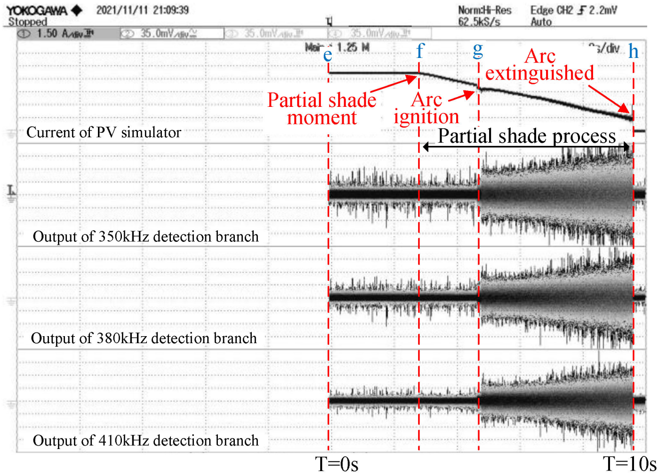

Fig. 42. Influence of irradiation change during arc fault on the outputs of three detection branches.

The third group of experiments set the PV simulator to the dynamic maximum power point tracking (MPPT) test mode, and the setting interface is shown in Fig. 41. In this experiment, the irradiation decreased from 1000 to 200 W/m^2, creating an arc fault as the irradiation decreased. In the meantime, the current and outputs of the three detection branches were collected. Then, the algorithm proposed in this article was used to identify arc faults. The purpose of this group was to verify whether irradiation changes influence the effectiveness of the proposed method. The results are shown in Figs. 42 and 43. As seen in those figures, during the irradiation fall, the algorithm quickly raises a fault alarm when an arc fault occurs. The results prove that irradiation change will not affect the effectiveness of the proposed detection method and will not cause misjudgment. The arc fault disappears because of the low current caused by low irradiation at 9.7 s, while the detection algorithm cancels fault alarms after the arc fault vanishes.

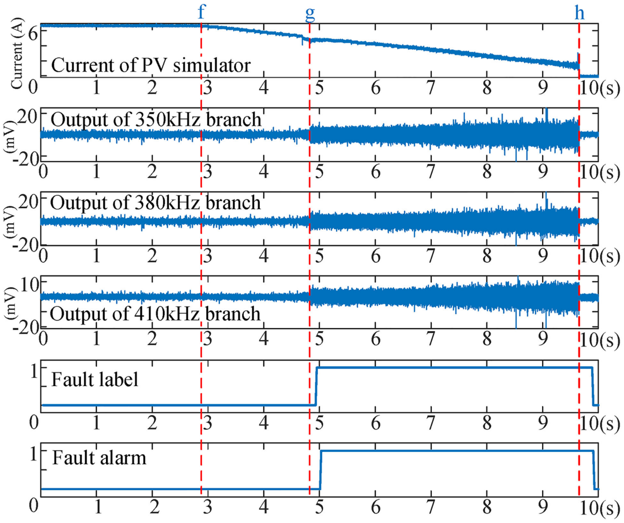

Fig. 43. Influence of irradiation change during arc fault on detection algorithm.

VI. CONCLUSION

The traditional current-based arc fault detection methods require high-performance hardware, such as wideband current sensors, fast data processors, and data acquisition cards. This increases the cost greatly. To address this shortcoming, this article chooses the CMCV signal as the research subject and designs a series of hardware circuits and arc fault detection software. The analysis and experimental results show the following.

1) Arc fault at any point in the PV string can be detected by monitoring the CMCV signal of the PV string power line at the terminal of the grid-connected inverter or PV combiner box, overcoming the difficulty of test point setting in differential-voltage signal detection methods. Moreover, this eliminates the limited bandwidth sensor problem in common current-based arc fault detection approaches.
2) Multiple frequency selection and detection hardware circuits are used to perform feature component extraction and frequency reduction, and the frequency components are concentrated at 0–20 kHz after reducing the frequency. Therefore, low- and medium-performance data processors can be applied to the AFDD. Therefore, the scheme proposed in this article has significant practical engineering value.
3) This article proposes a kind of arc similarity judgment algorithm based on the Euclidean distance that has higher accuracy in situations of few samples than common arc fault detection methods, such as wavelet-SVMs and wavelet-FFNNs. To some extent, the method proposed in this article has universality.
4) The arc fault detection method proposed in this article has good detection speed and the capability of avoiding flash arcs produced by dc switch operations, which are regulated by the UL1699B standard. Because the characteristic frequency band of the arcing CMCV signal chosen in this article is 300–500 kHz, avoiding the band of electronic noise, the interference of the power electronic device will not greatly affect the arc fault diagnosis method proposed in this article. In addition, load or irradiation change under arc situations will not influence the detection branches and algorithm, load or irradiation change under normal situations will not cause misjudgment of the proposed method, and load or irradiation change will not affect the effectiveness of the proposed detection method. It still has relatively high reliability when subjected to interference.

REFERENCES

[1] X. Yao, L. Herrera, S. Ji, K. Zou, and J. Wang, “Characteristic study and time-domain discrete-wavelet-transform based hybrid detection of series DC arc faults,” *IEEE Trans. Power Electron.*, vol. 29, no. 6, pp. 3103–3115, Jun. 2014.

[2] W. Chunhua, X. Wenxin, L. Zhihua, and X. Lijuan, “Arc type identification and circuit protection of DC side fault in photovoltaic system,” *Proc. CSEE*, vol. 37, no. 17, pp. 5028–5036, Sep. 2017.

[3] Z. Wang and R. S. Balog, “Arc fault and flash detection in photovoltaic systems using wavelet transform and support vector machines,” in *Proc. IEEE 43rd Photovolt. Specialists Conf.*, 2016, pp. 3275–3280.

[4] C. He, L. Mu, and Y. Wang, “The detection of parallel Arc fault in photovoltaic systems based on a mixed criterion,” *IEEE J. Photovolt.*, vol. 7, no. 6, pp. 1717–1724, Nov. 2017.

[5] H. Zhu, Z. Wang, and R. S. Balog, “Real time arc fault detection in PV systems using wavelet decomposition,” in *Proc. IEEE 43rd Photovolt. Specialists Conf.*, 2016, pp. 1761–1766.

[6] W. Dong, J.-M. Zhang, M.-J. Gui, and C.-G. Li, “Identification of aviation arc fault based on wavelet packet decomposition,” *Adv. Technol. Elect. Eng. Energy*, vol. 37, no. 11, pp. 76–81, Nov. 2018.

[7] Z.-J. Jiao, T. Li, L.-N. Wang, L.-H. Mu, and A. Khalyasmaa, “DC series arc-fault detection of photovoltaic system based on convolutional neural network,” *Adv. Technol. Elect. Eng. Energy*, vol. 38, no. 7, pp. 29–34, Jul. 2019.

[8] Q. Xiong, S. Ji, L. Zhu, L. Zhong, and Y. Liu, “A novel DC arc fault detection method based on electromagnetic radiation signal,” *IEEE Trans. Plasma Sci.*, vol. 45, no. 3, pp. 472–478, Mar. 2017.

[9] J. A. Momoh and R. Button, “Design and analysis of aerospace DC arcing faults using fast Fourier transformation and artificial neural network,” in *Proc. IEEE Power Eng. Soc. Gen. Meeting*, 2003, vol. 2, pp. 788–793.

[10] M. H. Riza Alvy Syafi’i, E. Prasetyono, M. K. Khafidli, D. O. Anggriawan, and A. Tjahjono, “Real time series DC arc fault detection based on fast Fourier transform,” in *Proc. Int. Electron. Symp. Eng. Technol. Appl.*, 2018, pp. 25–30.

[11] X. Cao, L. Dong, N. Huai, S. Liu, and H. Ma, “Detection of DC series arc fault in SSPC based on VMD and Shannon entropy criterion,” in *Proc. 37th Chin. Control Conf.*, 2018, pp. 5877–5883.

[12] N. L. Georgijevic, M. V. Jankovic, S. Srdic, and Z. Radakovic, “The detection of series arc fault in photovoltaic systems based on the arc current entropy,” *IEEE Trans. Power Electron.*, vol. 31, no. 8, pp. 5917–5930, Aug. 2016.

[13] W. Miao, Q. Xu, K. H. Lam, P. W. T. Pong, and H. V. Poor, “DC arc-fault detection based on empirical mode decomposition of arc signatures and support vector machine,” *IEEE Sensors J.*, vol. 21, no. 5, pp. 7024–7033, Mar. 2021.

[14] W. Chunhua, X. Wenxin, L. Zhihua, X. Lijuan, and B. Tongyang, “Research on DC arc fault detection method for photovoltaic system and its anti-interference,” *Proc. CSEE*, vol. 38, no. 12, pp. 3546–3554, Jun. 2018.

[15] Z. Yin, L. Wang, and Y. Zhang, “The detection of DC arc fault based on DFA,” in *Proc. IEEE Int. Conf. Prognostics Health Manage.*, 2018, pp. 1–6.

[16] S. Lu, T. Sirojan, B. T. Phung, D. Zhang, and E. Ambikairajah, “DA-DCGAN: An effective methodology for DC series arc fault diagnosis in photovoltaic systems,” *IEEE Access*, vol. 7, pp. 45831–45840, Apr. 2019.

[17] W. Chunhua, F. Xiayun, Y. Tonghao, L. Zhihua, and Z. Yang, “Research on PV fault arc detection method based on BP neural network,” *Acta Energiae Solaris Sinica*, vol. 37, no. 11, pp. 2958–2964, Nov. 2016.

[18] J. Yang and Y. Wang, “Identification and detection of DC arc fault in photovoltaic power generation system,” in *Proc. Int. Conf. Intell. Transp., Big Data Smart City*, 2020, pp. 440–444.

[19] K. Xia et al., “Wavelet entropy analysis and machine learning classification model of DC serial arc fault in electric vehicle power system,” *IET Power Electron.*, vol. 12, no. 15, pp. 3998–4004, Dec. 2019.

[20] K. Xia, S. He, Y. Tan, Q. Jiang, J. Xu, and W. Yu, “Wavelet packet and support vector machine analysis of series DC ARC fault detection in photovoltaic system,” *IEEJ Trans. Elect. Electron. Eng.*, vol. 14, no. 2, pp. 192–200, Feb. 2019.

[21] K. Li, S. Zhao, and Y. Wang, “A planar location method for DC arc faults using dual radiation detection points and DANN,” *IEEE Trans. Instrum. Meas.*, vol. 69, no. 8, pp. 5478–5487, Aug. 2020.

[22] V. Makarenko and V. Pilinsky, “The influence on the conductive interference operation mode of the magnetic core,” in *Proc. IEEE 39th Int. Conf. Electron. Nanotechnol.*, 2019, pp. 847–846.

[23] W. Fenz, S. Thumfart, R. Yatchak, H. Roitner, and B. Hofer, “Detection of arc faults in PV systems using compressed sensing,” *IEEE J. Photovolt.*, vol. 10, no. 2, pp. 676–684, Mar. 2020.

[24] G.-S. Seo, K. A. Kim, K.-C. Lee, K.-J. Lee, and B.-H. Cho, “A new DC arc fault detection method using DC system component modeling and analysis in low frequency range,” in *Proc. IEEE Appl. Power Electron. Conf. Expo.*, 2015, pp. 2438–2444.

Haining Wang received the B.Sc. degree in automatic engineering from the Hebei University of Technology, Handan, China, in 1999, and the Ph.D. degree in electrical engineering, with a specialization in photovoltaic generation, from the Hefei University of Technology, Heifei, China, in 2005.

She was a Postdoctoral Fellow with the Curtin University of Technology, Bentley, WA, Australia, from 2008 to 2009. She is currently an Associate Professor with the School of Electrical Engineering and Automation, Hefei University of Technology. Her current research interests include grid-connected inverter control, windand solar power generation, and distribution systems.

Xiaozhou Wang received the B.Eng. degree in electrical engineering from Anhui Polytechnic University, Wuhu, China, in 2019. He is currently working toward the M.Sc. degree with the Hefei University of Technology, Hefei, China.

His current research interests include renewable energy and power generation technology.

Tao Fan received the M.Sc. degree from Shandong University, Jinan, China, in 1996.

He worked in automation and informatization with Beijing Kedong Company, Beijing, China, and China Electric Power Research Institute and State Grid Electronic Commerce, Company, Ltd. He is currently a Professorate Senior Engineer and the Deputy Director of the Internet Department, State Grid Corporation of China, Beijing, China. His research interests include power system automation and energy interconnection.

Jian Wang was born in Tianjin, China. He received the B.Eng. degree from the Shenyang Institute of Engineering, Shenyang, China, in 2008.

He is currently a Senior Engineer with Tianjin Electric Power Science and Research Institution, State Grid Tianjin Electric Power Company, Tianjin, China. His current research interests include analysis of energy consumption and economic index of large power station, operation optimization technique, generator grid-related safety technology, and application and research of new energy technology and grid-power source coordination.

Zijie Lin was born in Zunyi, Guizhou, on November 1, 1997. He received the B.E. degree from the Faculty of Materials Science and Engineering, University of Science and Technology Beijing, Beijing, China, in 2019, and the M.Sc. degree in financial mathematics from the Faculty of Science and Physics, The University of Queensland, Brisbane, QLD, Australia, in 2021.

He was a Research Assistant with the University of Queensland, and a Research and Development Assistant Engineer with Beijing Benz Automotive, responsible for the localization of the cars and the optimization of the database. He is currently a Research Assistant with the Department of Finance, School of Economics and Management, Tsinghua University, Beijing, China. One of his research and development fields is “Forestry Carbon Sequestration.” Another is new energy grid-connected power generation technology.

Yu Shen was born in Huanggang, China, in 1998. She received the B.Sc. degree from the Faculty of Electronic and Electrical Engineering, Wuhan Textile University, Wuhan, China, in 2020. She is currently working toward the M.Sc. degree with the Hefei University of Technology, Hefei, China.

Her current research interests include electrical engineering.

Jianhui Su received the B.Sc., M.Sc., and Ph.D. degrees in electrical engineering from the Hefei University of Technology, Hefei, China, in 1984, 1987, and 2003, respectively.

He is currently a Full Professor with the School of Electrical Engineering and Automation, Hefei University of Technology, and an Associate Director of the Research Center for Photovoltaic System Engineering, Ministry of Education, Hefei, China. His research interests include renewable power generation, special power supply, distributed power generation systems, and high-voltage transducer control technologies.

Peng Zhang (Member, IEEE) received the B.Sc. degree in computer engineering from the Hebei University of Technology, Handan, China, in 1999, and the Ph.D. degree in electrical engineering from the Hefei University of Technology, Hefei, China, in 2020.

He is currently a Senior Experimentalist with the School of Electrical Engineering and Automation, Hefei University of Technology. His current research interests include distributed power generation and microgrid control.